Cold Regions Science and Technology 79-80 (2012) 20–28

Contents lists available at SciVerse ScienceDirect

Cold Regions Science and Technology

journal homepage: www.elsevier.com/locate/coldregions

A field study on failure of storm snow slab avalanches

Edward H. Bair [a,*], Ron Simenhois [b], Karl Birkeland [c], Jeff Dozier [a]

[a] US Army Corps of Engineers, Cold Regions Research and Engineering Laboratory, Hanover NH and Earth Research Institute, University of California, Santa Barbara, CA, USA
[b] Southeast Alaska Avalanche Center, Juneau, AK, USA
[c] US Forest Service National Avalanche Center, Bozeman, MT, USA

ARTICLE INFO

Article history:
Received 24 November 2011
Accepted 24 February 2012

Keywords:
Snow
Avalanche
Anticrack

ABSTRACT

Storm snow often avalanches before crystals metamorphose into faceted or rounded shapes, which typically occurs within a few days. We call such crystals nonpersistent, to distinguish them from snow crystals that persist within the snowpack for weeks or even months. Nonpersistent crystals can form weak layers or interfaces that are common sources of failure for avalanches. The anticrack fracture model emphasizes collapse and predicts that triggering is almost independent of slope angle, but this prediction has only been tested on persistent weak layers. In this study, dozens of stability tests show that both nonpersistent and persistent crystals collapse during failure, and that slope angle does not affect triggering (although slope angle determines whether collapse leads to an avalanche). Our findings suggest that avalanches in storm snow and persistent weak layers share the same failure mechanism described by the anticrack model, with collapse providing the fracture energy. Manual hardness measurements and near-infrared measurements of grain size sometimes showed thin weak layers of softer and larger crystals in storm snow, but often showed failures at interfaces marked by softer layers above and harder layers below. We suggest collapse often occurs in crystals at the bottom of the slab. Planar crystals such as sectored plates were often found in failure layers, suggesting they are especially prone to collapse.

1. Introduction

1.1. Storm snow crystals

Crystals in storm snow typically metamorphose into rounded or faceted shapes within three days, so we call them nonpersistent, whereas persistent crystals maintain their form even deep within the snowpack and can remain unstable for weeks or months. Avalanches that fail on persistent crystals cause more fatalities than those that fail on nonpersistent crystals (Jamieson and Johnston, 1992) because they are more difficult to predict and involve deeper and harder slabs. Yet, avalanches that fail on nonpersistent crystals are also common, have killed at least 25 people in the U.S. since 1998–1999, and are responsible for the majority of deaths in some U.S. states (Fig. 1).

In half of all U.S. avalanche fatalities, failure crystals are not known. Because avalanches on nonpersistent crystals occur during storms and are therefore difficult to document, we suggest that they are more often classified as “unknown failure crystal” than those on persistent crystals. The two paragraphs below describe large avalanche events that probably failed in storm snow rather than an older, deeper layer. Crown face profiles were not examined in either case because of extreme avalanche danger.

On 31 Mar 1982, a massive natural avalanche released after control work at Alpine Meadows ski area in California. The avalanche destroyed two buildings and killed seven people in the parking lot and base area. At the time of the accident, the storm had deposited 2.2 m of snow on a well bonded melt-freeze crust. Strong Sierra Nevada winds up to 192 km/h increased snow on the slope, so crown heights ranged from 2 to 3 m (Penniman, 1986). Although a definitive failure crystal cannot be ascribed, the slab in the fatal avalanche probably involved only storm snow and failed on nonpersistent crystals.

February 1999 was the deadliest month for avalanche fatalities in recent history for the European Alps. Avalanches killed 59 people, 15 in the French Alps where eye-witnesses said that most avalanches involved storm snow only. Sensitivity tests show that observed avalanche hazard and run outs could be simulated without a pre-existing weak snowpack, suggesting the fatal avalanches failed on nonpersistent crystals (Rousselout et al., 2010; Villecrose, 2001).

Avalanches that fail on persistent crystals have been the topic of many studies, while little is known about avalanches that fail on nonpersistent crystals.

1.2. Applying the anticrack model to fracture of nonpersistent crystals

The anticrack snow fracture model (Heierli et al., 2008) emphasizes collapse and predicts that triggering fracture is almost independent of slope angle, but verification has been solely with failures on persistent crystals, so the model's applicability to nonpersistent crystals is unclear. In our field experience, crystals in storm snow are smaller, their failures often do not propagate as far, and they tend to cause smaller avalanches than persistent crystals. Because simple

* Corresponding author.
E-mail address: nbair@eri.ucsb.edu (E.H. Bair).

0165-232X/$ – see front matter © 2012 Elsevier B.V. All rights reserved.
doi:10.1016/j.coldregions.2012.02.007

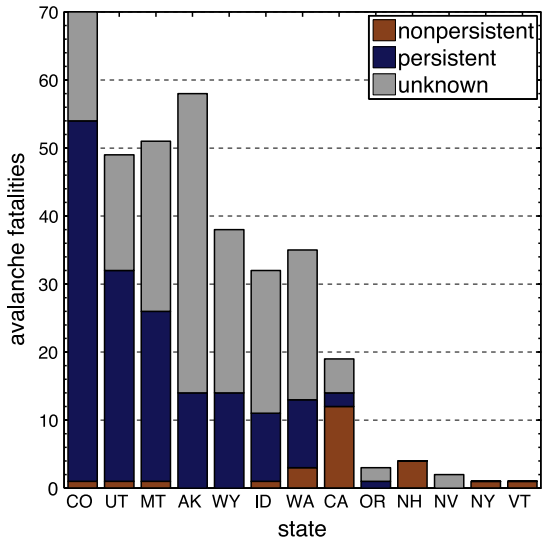

Fig. 1. U.S. avalanche fatalities by state and failure crystal from 1998 to 2011 (American Avalanche Association, 2011).

shear models cannot explain the reality of remotely triggered avalanches in storm snow, a fundamental question arises: Does the anticrack model apply to avalanches within storm snow?

2. Literature review

A significant portion of snow avalanche research since the late 1970s focuses on applying fracture mechanics to snow avalanches. The following sections present an overview of two types of models, simple shear models and the anticrack model.

2.1. Simple shear models

Early work (McClung, 1979, 1981) applied shear models from soils (Palmer and Rice, 1973) to snow. For natural avalanches in the simple shear model, a weak layer at thickness D from the surface is overlaid by a stronger slab. This weak layer is assumed to have flaws of size r, which are unstable if r exceeds the critical flaw size r_c. According to McClung (1979):

$$r_c = \sqrt{2D\frac{w_f E}{(\tau-\tau_r)^2}} \tag{1}$$

The expression $\tau-\tau_r$ is the shear stress τ at the weak layer reduced by residual crack-face friction τ_r. Shear stress $\tau=\rho g D \sin\theta$ and $\tau_r = min[\tau, \mu(\rho g D \cos\theta)]$. Fracture energy is w_f, ρ is slab density, E is the elastic modulus, θ is slope angle, and μ is the coefficient of friction. As long as $r<r_c$, self-sustaining crack propagation will not occur. In natural avalanches, there are two ways r can become critical: a decrease in r_c caused by increased loading from precipitation or an increase in r caused by metamorphism. Once r becomes critical:

1. The flaw will spontaneously and rapidly grow in slope parallel (mode II) and anti-parallel (mode III) directions.
2. Propagating longitudinal waves build tension at the crack tip as the length of propagation $l \gg D$.
3. At $l = (20\ to\ 40)D$, tensile stresses approach mode I fracture toughness of the slab. Tensile stress increases toward the bottom of the slab from a lack of friction between the slab and the failed weak layer (McClung, 2009; McClung and Schweizer, 2006). A crown fracture forms, with the crack hypothesized to travel from the bed to the snow surface (McClung, 2005).
4. Flank and then stauchwall failure follow the crown fracture, after a large enough area has been cut out by steps 1–3.

In this and other shear models for snow (Bažant et al., 2003; Chiaia et al., 2008; Louchet et al., 2002), there is a negative relationship between θ and r_c; r_c increases with decreasing slope angle to the point where shear cracks cannot propagate. In Eq. (1), r_c is undefined for $\tau-\tau_r=0$, i.e. whenever the slope angle is less than the friction angle. According to Heierli et al. (2008), shear models cannot explain remote triggering (Johnson, 2001) or Propagation Saw Tests on persistent crystals that show r_c is invariant or increases slightly with slope angle (Gauthier and Jamieson, 2008). Likewise, Extended Column Tests on persistent crystals show that scores are invariant or increase slightly with slope angle (Heierli et al., 2011). Further, high speed video measurements show that slope normal collapse preceding slope parallel acceleration is the rule rather than the exception in slab avalanches (van Herwijnen and Jamieson, 2005; van Herwijnen et al., 2010).

2.2. Mixed-mode anticrack model

Fracture models that account for volumetric collapse of snow have been developed to address shear model deficiencies (Heierli, 2008; Heierli et al., 2008; Johnson, 2001). Pre-eminent is the anticrack model (Heierli et al., 2008). An anticrack is the opposite of a tensile (mode I) crack. Like all fracture mechanical models for snow, the anticrack model assumes sub-critical flaws of radius r in a weak layer, overlaid by a slab of thickness D. Flaws can become critical from three mechanisms: an artificial trigger, increasing load from precipitation, or a loss of strength caused by metamorphism. However, in the anticrack model, r_c is almost independent of slope angle under two conditions: i) $\theta<60°$ and ii) D decreases with $\cos\theta$. Assuming a similar slab and substrate, an expression for r_c for natural avalanches is (Heierli et al., 2008):

$$r_c \propto \frac{w_f E}{\pi(\rho g D)^2} \tag{2}$$

Once r becomes critical, cracks in the weak layer will spread as a mixed-mode (anticrack mode and mode II) collapse wave, where bending and collapse of the slab provide fracture energy. In homogenous flat snowpacks at high latitudes, collapse waves — called “firn quakes” (Johnson et al., 2004) — have been observed to travel for kilometers.

In seasonal snow with high spatial variability, the collapse wave can be arrested by a variety of mechanisms. After collapse and propagation, according to Heierli et al. (2008), the amount of friction between the collapsed failure layer and the slab determines whether the slab will slide downhill or whether it collapses and does not slide, in which case it makes a distinctive sound, the onomatopoetic “whumpf.”

3. Methods and datasets

3.1. Snow pits, Propagation Saw Tests, and Extended Column Tests

During the accumulation season of 2010–2011, we dug snow pits and performed stability tests at two locations: Mammoth Mountain, CA and Kakauan, AK (Table 1). Standard snow pit measurements for each layer included depth, hand hardness, crystal form/size, and density. A general snow temperature was sometimes measured, but detailed layer temperatures were usually not. Temperature of the storm snow was often nearly the same as the air temperature. Other measurements included air temperature, aspect, and weather conditions. For hand hardness (Fierz et al., 2009), plus (+) corresponds to 0.5, and minus (−) to −0.2. For interface failures, failure layer refers to the layer immediately above the interface since, in all cases, that layer was softer than the layer below the interface.

Table 1
Snow pit measurements for Propagation Saw Tests and Extended Column Tests.

Date	Location	Slope angle θ, °	Slab thickness D, cm	Failure layer hand hardness	Failure layer crystal size, mm	Failure layer crystal form	Layer above hand hardness	Layer below hand hardness
21 Nov 2010	CA	NA	NA	NA	NA	+	NA	NA
6 Dec 2010	CA	45	42	3.0	1.0–1.5	*	1.5	3.0
20 Dec 2010	CA	40	40	1.0	NA	+	1.0	1.8
20 Jan 2011	AK	14–38	16–24	1.0	NA	+	2.5	2.0
16 Feb 2011	CA	34	34	1.0	0.5–1.0	□ ⟋	3.5	3.0
16 Feb 2011	AK	8–43	20–29	1.5	2.0	+	2.8	2.0
19 Mar 2011	CA	25–45	26–30	0.8	1.0–2.0	*	1.0	2.0
20 Mar 2011	CA	45	33	1.0	1.0	⊙ *	1.0	2.0

Notes: Location — AK is Kakauan, AK, CA is Mammoth Mountain, CA, crystal form and hand hardness are from the International Classification for Seasonal Snow on the Ground (Fierz et al., 2009), slab thickness D is measured slope normal, NA is not applicable/not measured.

Propagation Saw Tests (PST) followed procedures and recording standards in Gauthier and Jamieson (2008), except that column ends were slope normal, rather than vertical. Slope normal column ends give r_c values that are equivalent to those in Heierli et al. (2008) without needing additional corrections. Columns were 1.0–1.2 m long in the upslope direction. Only fractures that reached the end of the PST column are analyzed in this study.

Extended Column Tests (ECT) followed procedures and recording standards in Simenhois and Birkeland (2009). Like the PSTs, only fractures that traveled completely across the column are analyzed in this study. We choose to only include PSTs and ECTs with fractures that reached the end of the column because these are associated with avalanches and other signs of instability (Schweizer and Jamieson, 2010), such as "whumpfing." It is usually easy to trigger cracks that do not propagate in storm snow, since it is among the weakest of all types (Roch, 1966). Whether a fracture propagates across the block is the key factor in determining whether or not slab avalanches are likely.

3.2. Applying shear and anticrack models to measured critical cut lengths

Critical cut length r_c values were computed using a shear model and the anticrack model to compare with measured r_c values. These r_c values apply to natural avalanches, since there is no external load, only the weight of the slab. Since the slabs were unsupported behind the saw blade, residual friction τ_r is zero and application of the shear model comes directly from Eq. (1). Use of a thick (5 mm) snow saw and analysis of slope normal displacement of the slab prior to fracture ensured that there was no crack-face contact, which would bias measured r_c.

Fracture mechanical parameters are mean values from two PSTs the next day with similar new snow, $w_f = 0.08\,J\,m^{-2}$ and $E = 0.22\,MPa$, measured using a new technique based on bending of the slab prior to propagation (van Herwijnen and Heierli, 2010). To find r_c using the anticrack model, Eq. (4.13) from Heierli (2008) is maximized:

$$V(r,E) = w_f r - \frac{\pi\gamma r^2}{4E}\left[\tau^2+\sigma^2\right] - \frac{r^3}{6ED}\left[\lambda_{\tau\tau}(r)\tau^2 + \lambda_{\sigma\tau}(r)\sigma\tau + \lambda_{\sigma\sigma}(r)\sigma^2\right] \tag{3}$$

where

$$\lambda_{\tau\tau}(r) = 1 + \frac{9}{4}\eta\left[\frac{r}{D}\right]^{-1} + \frac{9}{4}\eta^2\left[\frac{r}{D}\right]^{-2} \tag{4}$$

$$\lambda_{\sigma\tau}(r) = \frac{9}{2}\eta + \frac{9}{2}\eta^2\left[\frac{r}{D}\right]^{-1} \tag{5}$$

$$\lambda_{\sigma\sigma}(r) = 3\eta^2 + \frac{9}{4}\eta\left[\frac{r}{D}\right] + \frac{9}{5}\left[\frac{r}{D}\right]^2 \tag{6}$$

The elastic constant is η, assumed here to be 1 for a Poisson solid (Poisson number 0.25), a reasonable approximation for storm snow. The mismatch parameter is γ, also assumed to be 1, given similar snow above and below the fracture path. A constant value (0.35 m) of slab height H, measured vertically, was multiplied by $\cos\theta$ for D.

3.3. Particle tracking

3.3.1. Propagation Saw Tests

For two PSTs (6 Dec 2010 and 16 Feb 2011 at Mammoth Mountain in Table 1), black markers, 35 mm in diameter, were inserted into the column so that its movement could be analyzed (Fig. 2). These were the only tests suitable for measuring collapse amplitude a, since the slab collapsed but stopped sliding downhill. For tests where the slab collapses and continues to slide downhill, bed surface erosion superposes the collapse amplitude (van Herwijnen and Jamieson, 2005).

The video camera used was a Canon G10 shooting 640×480 frames at 30 Hz. The focal length of the lens is 28–140 mm at 35 mm film equivalent. Videos were shot at around 50 mm focal length to minimize barrel distortion but also provide a wide enough field of view to capture the entire column.

Prior to sawing, careful measurments of slab width w, length l, and thickness D were taken at multiple places to ensure consistent proportions. If one side of the slab was wider or the walls were not perpendicular to the ground, it was carefully shaved down with a shovel. Inclination of the column was measured at several locations on the snow surface with a Brooks Range inclinometer and/or a Suunto inclinometer. Based on measurments with both instruments, the slope angle accuracy is estimated to be ±1°.

3.3.2. Analysis

Videos were imported into MATLAB for analysis. Custom functions were written utilizing open-source particle tracking software (Crocker and Grier, 1996). The method presented here closely follows procedures in van Herwijnen and Jamieson (2005) and van

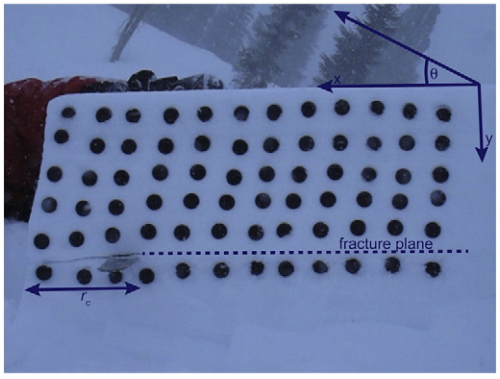

Fig. 2. Propagation Saw Test with particle tracking markers inserted to measure movement, Mammoth Mountain, 16 Feb 2011 (Table 1).

Herwijnen et al. (2010). In the tests, distortion from perspective was negligible, so it was not corrected.

Videos were inverted (black markers become white) and contrast was increased. A 2-d bandpass filter was applied to smooth noise. The bandpass filter was followed by two successive functions to locate and refine estimates of particle center coordinates. Once the center coordinates were estimated for markers in each frame, they could be tracked using a tracking function. Ultimately, a list of marker centroid pixel positions, called trajectories, was produced over the frames of analysis. A nine-frame averaging filter was applied to the trajectories in order to further reduce noise from artifacts such as pixel clipping (van Herwijnen and Jamieson, 2005; van Herwijnen et al., 2010).

3.3.3. Displacement measurements

From the list of trajectories, it was simple to compute slope parallel $u_x(t)$ and slope normal $u_y(t)$ displacements in the slope rotated coordinate system:

$$u_x(t) = x(t) - x(0),\ u_y(t) = y(t) - y(0) \tag{7}$$

where $x(t)$ and $y(t)$ are slope parallel and slope normal positions at time t in sec.

The initial positions $x(0)$ and $y(0)$ were determined by averaging marker positions 50 frames prior to sawing, thereby eliminating noise caused by changes in illumination or thermal fluctuations of the CCD (van Herwijnen et al., 2010). A mean standard deviation of marker movement prior to sawing was computed and used as an error estimate of position. In addition, for a small error in measurement angle, coordinate rotation leads to uncertainty in displacement from slope angle:

$$\delta u_y = \delta y + \delta\theta u_x \tag{8}$$

where δu_y is the total uncertainty in slope normal displacement, δy is the contribution from uncertainty in position, $\delta\theta u_x$ is the contribution from uncertainty in slope angle, and $\delta\theta = \pm 0.017\ rad$ is the uncertainty in slope angle. To track slope normal displacement of the entire slab, an average of $u_y(t)$ was used. Collapse amplitude a is the asymptotic value of $u_y(t)$ after the slab stops moving.

3.4. Crown profiles

Twenty crown profiles, taken over nine seasons, of avalanches at Mammoth Mountain that failed in storm snow were analyzed. Detailed crown profiles conducted by three different experienced observers were generally completed within 24 h of the avalanche. As with most crown face profiles, they are skewed towards larger and more impressive avalanches (Perla, 1977; Stethem and Perla, 1980). As with interface failures from the stability tests, failure layer refers to the layer immediately above the fracture, since it was also the softer layer in all cases.

3.5. Near-infrared imaging

3.5.1. Preparation of snow pit wall

Methods for near-infrared imaging are based on techniques presented by Matzl (2006) and Matzl and Schneebeli (2006). First, we planed the pit wall to be as smooth as possible using a very flat shovel blade. It is critically important that the pit wall be smooth; otherwise differences in refectance caused by small ridges will appear in the final nIR image. Since most tests took place in heavy snow or high winds, we shielded the pit wall from falling and blowing snow with an umbrella. The umbrella also diffused light on the few days with direct sunlight.

Since there is less sunlight available at near-infrared wavelengths, exposure times are longer and a tripod must be used to prevent camera movement. Images were taken at a distance of 1 to 2 m from the column. For each sample, the camera was carefully positioned to be parallel with the column and at the same slope angle (Fig. 2).

3.5.2. Image of snow pit wall

The first nIR image was of the snow pit wall framed by Spectralon targets with 50% and 99% reflectance. The camera's CMOS detector is sensitive to wavelengths from 330–1200 nm, but a filter limits the sensitivity to 850–1200 nm. A second nIR image was of a flat white foam placed in front of the snow. The white background is used to correct for the "hotspot" or vignetting effect that seems to be present in most nIR images (Tape et al., 2010). Since most camera lenses are optimized for the visible spectrum, they have coatings on the internal lens elements that are not efficient in near-infrared wavelengths. These coatings cause nIR light to be reflected rather than refracted and can cause a series of internal reflections that amplify light at the center of the sensor and cause a hot spot. Lenses exist with coatings and focus optimized for use at nIR wavelengths, but they are considerably more expensive than most visible light camera lenses.

3.5.3. Analysis

The technique for post-processing nIR images is primarlily from Matzl (2006) and Matzl and Schneebeli (2006) with contributions from other nIR snow studies (Schneebeli, 2008; Tape et al., 2010). First, the two images were retrieved from the camera and brought into an application capable of processing RAW images, in this case Adobe Photoshop CS5. The tone curve was set to linear, so that the input/output values had a 1:1 correspondence. Standard sharpening and noise reduction were not applied. The green channel, which is most sensitive to the range of the filter, was then extracted and saved as a 16-bit grayscale image, although in practice the red and blue channels could have been used too.

Both TIFFs were imported into MATLAB. A corrected image C was created by normalizing the image of the targets T by the flat field image F and then multiplying by the mean of the entire flat field image $\bar{F}$ (Tape et al., 2010):

$$C_{ij} = \frac{\bar{F} T_{ij}}{F_{ij}} \tag{9}$$

where i and j are indices to each pixel. Once the corrected image was calculated, a linear regression between pixel intensity (digital number) and reflectance was made using the locations of the 50% and 99% reflectance Spectralon targets. The corrected image C was transformed into an image of reflectance R using the coefficients from the linear regression:

$$R_{ij} = b_1 + b_2 C_{ij} \tag{10}$$

An empirical relationship between reflectance and specific surface area, SSA (SSA = surface area/volume), was used to transform R into SSA (Matzl and Schneebeli, 2006).

$$SSA_{ij} = A\ exp\left(R_{ij}/B\right) \tag{11}$$

where $A = 0.02\ \mathrm{mm}^{-1}$ and $B = 12.22$. Finally, an effective spherical diameter d is:

$$d = 6/SSA \tag{12}$$

For precise estimate of grain size, the nIR image should be corrected for lens distortion and perspective. For examining potential fracture locations in nonpersistent crystals, however, the relative differences in d are more important than precise values, so the images

were not corrected for distortion. In most images, distortion from perspective was assumed small, as was barrel distortion.

4. Terminology

We use storm snow to refer to snow that falls during a continuous period of precipitation, which can last multiple days. We use new snow to refer to snow that fell with the last 24 h (Fierz et al., 2009).

The term layer is often used loosely, so we provide a precise definition. We use layer to refer to a volume of snow with the same properties, given the method of measurement. For traditional snow pit measurements, those properties are: hand hardness, crystal form and size, and density. For snow pits where nIR images were taken, in addition to the properties above, we add that a layer must have similar values and variability in reflectance.

We use two basic locations to describe where failure occurs, at a weak layer or at an interface. Weak layers, also called sandwich layers (Hutchinson and Suo, 1991), are often thin (a few cm) layers characterized by weak intra- and/or interlayer bonds. Weak layers are usually softer than layers above and below.

In many cases, failures occur between two layers without a discernible weak layer. These are called interface failures. Interface failures arise from weak interfacial bonds between two layers. In this case, Schweizer and Jamieson (2003) define the failure layer as the softer of the layers above or below the interface. For the stability tests and crown profiles, the softer layer was always above the interface.

5. Results

Probabilities in the results are based on the Kruskal-Wallis (1952) test, which assumes that populations have the same, not necessarily normal, distribution and that all observations are independent. The null hypothesis is that the two groups come from the same population. We use a threshold p value for significance at $p \leq 0.05$, below which the null hypothesis is rejected and the two groups are significantly different.

5.1. Slope angle independence for Propagation Saw Tests

To test the effect of slope angle on failures of nonpersistent crystals, nine PSTs were performed on 19 Mar 2011 on uniform slopes with θ from 25° to 45°. The error of the inclinometers is estimated to be $\pm 1°$ and the error of r_c is estimated to be ± 5 mm. Columns were 0.26–0.30 m thick, with no trend in thickness vs. slope angle, the columns were each 1.20×0.30 m, and the saw used is 5 mm thick. The assumption is that these small scale tests with isolated columns approximate the slab avalanche process. In reality, values for r_c are probably larger because avalanche slabs are supported on all four sides.

A simple shear model and the anticrack model are compared to the measured r_c values (Fig. 3), which do not depend on slope angle. For the slope angles measured, the anticrack model predicts r_c values of 0.06–0.07 m, while the shear model predicts r_c values that are an order of magnitude larger, 0.54–0.79 m. While the anticrack model predicts relatively constant r_c values, the shear model predicts decreasing r_c with increasing θ. Relatively constant r_c values with increasing θ are consistent with field measurements and anticrack model predictions of failures on persistent crystals (Gauthier and Jamieson, 2008; Heierli et al., 2008).

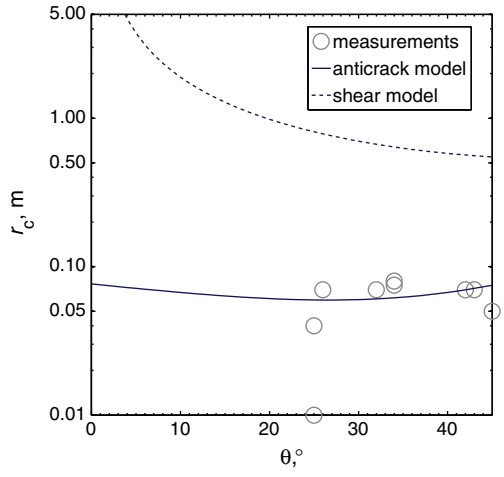

Fig. 3. Critical cut length r_c vs. slope angle θ, from Propagation Saw Tests. Fracture mechanical parameters used are: $w_f = 0.08\ J\ m^{-2}$, $E = 0.22\ MPa$, $\rho = 86\ kg\ m^{-3}$, $H = 0.35\ m$, $D = H \cos\theta$, and $\gamma = \eta = 1$.

5.2. Slope angle independence for Extended Column Tests

ECTs conducted on two sampling dates in Kakauan, AK show similar trends as the PSTs. The number of ECT taps until propagation is constant or slightly increases with slope angle (Fig. 4). These results are consistent with previous work showing ECT scores vary little with slope angle for failures on persistent crystals (Heierli et al., 2011). As with the PSTs, there is no trend in slope angle vs. slab thickness for either sampling date.

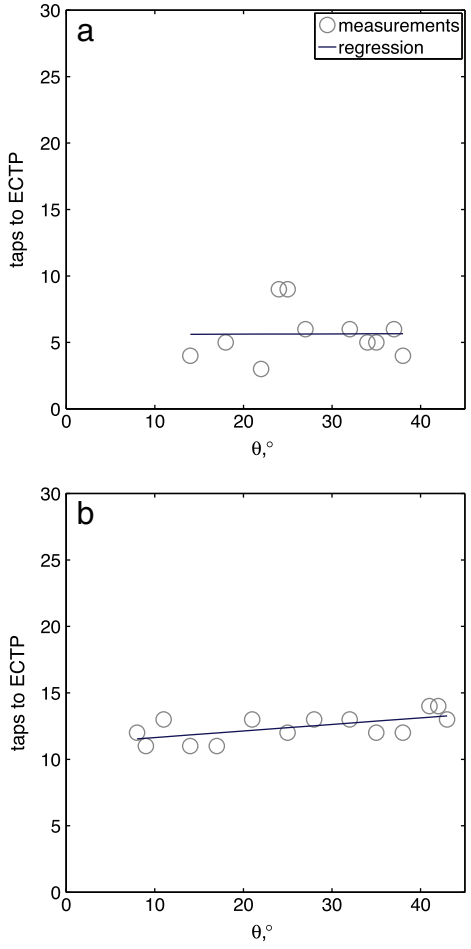

Fig. 4. Extended Column Tests from: (a) 20 Jan 2011 and (b) 16 Feb 2011. The vertical axis is the score when a fracture first crosses the column.

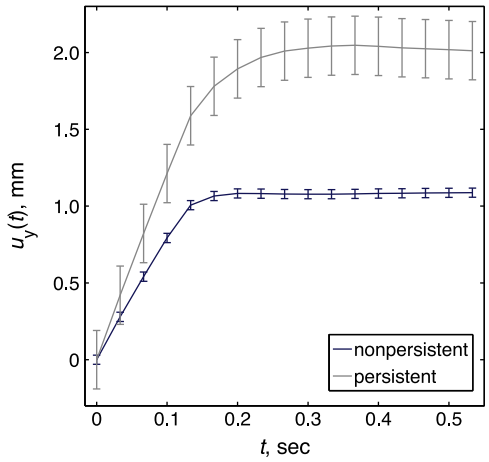

Fig. 5. Plots of slope normal displacement u_y for two slabs that collapsed, but did not continue to slide downhill. One slab failed on nonpersistent crystals (blue lines, 6 Dec 2010 in Table 1), the other on persistent crystals (gray lines, 16 Feb 2011, CA, in Table 1). Displacements are computed from average movement of all markers above the fracture.

5.3. Slope normal displacement

Collapse amplitude was measured for two failures, one on nonpersistent crystals and the other on persistent crystals (Fig. 5). Collapse amplitude for the failure on nonpersistent crystals is 1.08 ± 0.03 mm, vs. 2.03 ± 0.19 mm for the failure on persistent crystals.

5.4. Hand hardness from crown profiles

There is no significant hardness difference between the layer above (LA) and the failure layer (FL, Fig. 6). Hardness of the layer below (LB) is significantly greater. The median hand hardness for the failure layer is 2.5 vs. 3.8 for the layer below ($p<0.01$).

5.5. Nonpersistent crystals at failures

5.5.1. Crown profiles

At failure layers, plates (⊙) are the most common (47%) crystals found (Fig. 7). Also common are columns (□, 26%), wind packed crystals (◪, 26%), partly decomposed precipitation particles (/, 21%), and graupel (⧖, 21%). Other crystals comprise less than 20% of the total.

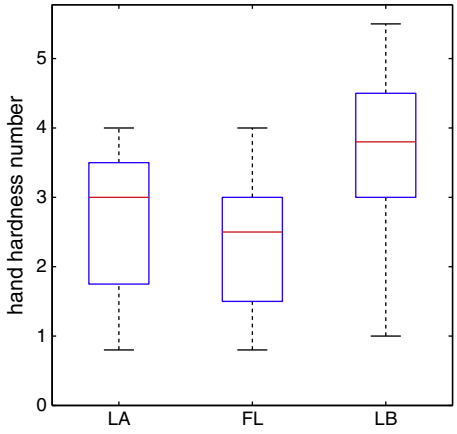

Fig. 6. Hand hardness for layer above (LA), failure layer (FL), and layer below (LB) for avalanches that failed on nonpersistent crystals. Line at center is the median, boxes are 25th and 75th percentiles, and whiskers are minima and maxima.

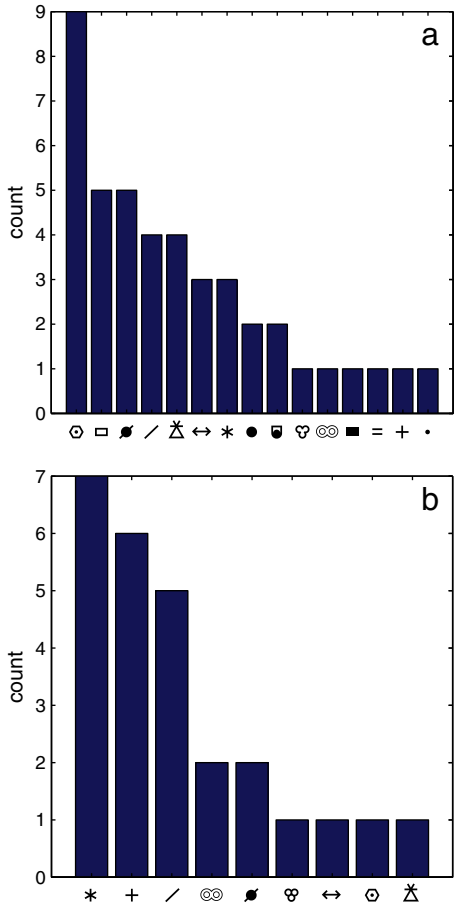

Fig. 7. Failure layer crystals: (a) crown profiles from avalanches on Mammoth Mountain; (b) stability tests from Mammoth Mountain during the 2010–2011 season. Vertical axis is the count (frequency) of times each crystal form was found. Crystal forms are: plates (⊙), columns (□), wind packed rounded grains (◪), partly decomposed precipitation particles (/), graupel (⧖), needles (↔), stellars (∗), large rounded particles (●), faceted rounded particles (◒), rounded polycrystals (✿), melt-freeze crust (◎), ice layer (■), rain crust (=), unspecified precipitation particles (+), small rounded particles (•), and clustered rounded grains (✿).

5.5.2. Stability tests

Dendrites (*) are in failures layers in half the stability tests (Fig. 7). Unspecified new snow particles (+) are also abundant (47%) because falling and blowing snow often made detailed crystal identification impossible. Decomposing precipitation particles (/) are also relatively abundant (36%). Other crystal types are present 15% or less of the tests.

5.6. Hand hardness and density from stability tests

Like the crown profiles, stability tests show layers below the failure layer (LB) are significantly harder ($p<0.01$), but also denser ($p=0.04$) than failure layers and layers above. The median hand hardness and density is 1.5 (fist +) and 120 kg m^{-3} vs. 2.7 (4 finger +) and 150 kg m^{-3} for layers below (Fig. 8). Layers above the failure layer are not significantly harder ($p=0.57$) or denser ($p=0.74$) than failure layers.

5.7. Near-infrared images

In some cases (Fig. 9b and c), thin weak layers with larger effective diameters than adjacent strata fractured in stability tests. Note that Fig. 9b actually has two weak layers at different depths. The deeper weak layer failed more easily than the upper weak layer. In other cases (Fig. 9a and d), there are no clear weak layers; fracture occurs

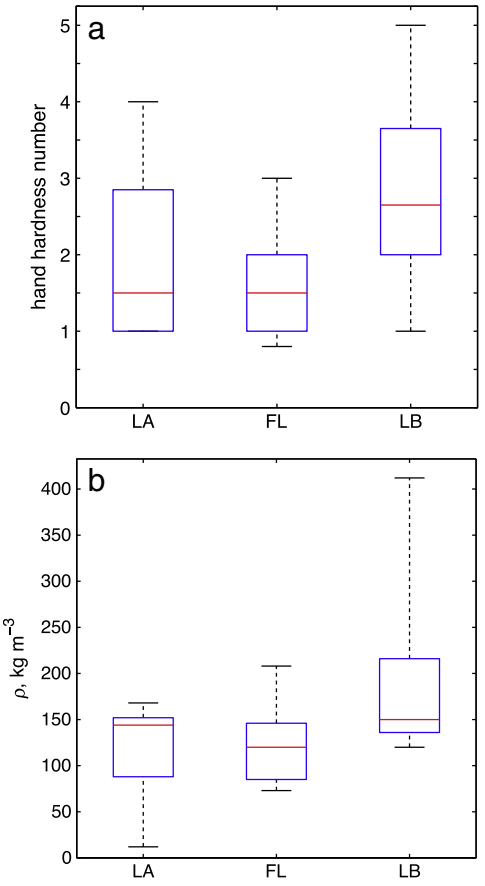

Fig. 8. (a) Hardness and (b) density for layer above, failure layer, and layer below in snow pits with stability tests. Right is the same, but for density.

at the bottom of the slab above slightly smaller (a) or slightly larger (d) grains. In both profiles without weak layers, grain sizes above are about the same as grain sizes at the failure.

For two of the three cases shown in Fig. 9 and Table 1 where hand hardness was recorded, (c: 20 Dec 2010, and d: 20 Mar 2011), failure layers show the same hardness trends as crown profiles. The layer above is the same hardness as the failure layer, while the layer below is harder. In one case (b: 6 Dec 2010), the layer above is actually softer than the failure layer, while the layer below is the same hardness.

6. Discussion

6.1. Slope angle independence for ECTs and PSTs on nonpersistent crystals

Using two different stability tests, Sections 5.1 and 5.2 show that slope angle had little effect on triggering fracture in nonpersistent crystals. Like previous work with failures on persistent crystals (Gauthier and Jamieson, 2008), r_c in Propagation Saw Tests shows little sensitivity to slope angle, in contrast to the decreasing r_c with slope angle predicted by the simple shear model.

Because the PST has been criticized for causing excess tension on the slab and artificially high collapse (McClung, 2011), an additional stability test of slope angle independence for triggering was necessary. The ECT also measures ease of triggering, but does not use an artificial gap as the loading technique. Instead, the ECT uses dynamic compressive stress, which more closely simulates how skiers or snowboarders trigger avalanches. These results, which also show little slope angle dependence for triggering on nonpersistent crystals, agree with previous studies that show similar trends with ECTs on persistent crystals (Heierli et al., 2011).

In contrast, Reiweger and Schweizer (2010) show decreasing stress at failure with increasing slope angle for a weak layer of surface hoar. They attribute these effects to the anisotropy of surface hoar crystals. Since they are randomly orientated, this finding is not applicable to nonpersistent crystals. Further, given their small sample size (125 mm in length), Reiweger and Schweizer are careful to say that their findings only apply to failure initiation, not crack propagation. Conversely, our study is concerned only with stability tests that cause propagation.

Previous studies show that collapse occurs on persistent crystals during various stability tests, including ski cutting, compression tests, and rutschblocks tests (van Herwijnen and Jamieson, 2005). Likewise, we show that collapse, required by the anticrack model, occurred on nonpersistent crystals in all measurements, regardless of the stability test used. Since both persistent and nonpersistent crystals showed little sensitivity to slope angle for triggering, our results suggest they share the same failure mechanism, driven by collapse.

6.2. Slope normal displacement

Although more measurements of collapse amplitude a are needed, these preliminary results show that nonpersistent crystals collapsed during failure, just as persistent crystals have been shown to. The measured values (~1 and 2 mm) are within the range of published values (1–40 mm) for failures on persistent crystals (Johnson, 2001; van Herwijnen and Jamieson, 2005; van Herwijnen et al., 2010). In previous studies, there is a positive relationship between crystal size in the failure layer and collapse amplitude. For instance, the largest (40 mm) reported collapse occurred on very large (30–40 mm) surface hoar crystals (van Herwijnen et al., 2010), while the smallest (1 mm) occurred on much smaller (3–7 mm) surface hoar crystals (Johnson, 2001). Crystals in the failure layer of the 6 Dec 2010 PST were manually classified as 0.5–1.0 mm stellars and partly decomposed particles (*/). Crystals in the failure layer of the 16 Feb 2011 PST were manually classified as 0.5–1.0 mm facets and wind-broken particles (□ ⁄). It is not possible to draw broad conclusions from two measurements of collapse amplitude, but our results show that greater collapse occurred on persistent crystals than on nonpersistent crystals of the same diameter. The small collapse amplitudes explain why nonpersistent crystals have been associated with planar fractures. For instance, failures on nonpersistent crystals were 2–3× more likely to have “planar” fracture character, rather than “collapse” character in compression tests (van Herwijnen and Jamieson, 2007). A heavier slab for the 16 Feb 2011 PST ($D = 25$ vs. 34 cm with equal density) could also be responsible for the greater collapse amplitude. The most important finding is that collapse amplitude for this test on nonpersistent crystals was small, but not negligible.

6.3. Hand hardness from crown profiles and stability tests

Crown profiles and stability tests show the same result. Nonpersistent crystals in failure layers were not significantly harder or softer than slabs above, but had significantly harder layers below. Stability tests also show significantly denser layers below. Densities were not consistently recorded in crown profiles, so they are not included. This result suggests that failure occurs at the interface between the softer and harder snow. Likewise, Schweizer and Jamieson (2001) found significantly harder layers below interface failures, which involve predominately nonpersistent crystals, for Canadian avalanches triggered by skiers. We conclude that the best way to locate a potential failure layer of nonpersistent crystals is to search for a harder layer below a slab of new snow. Fracture will most likely occur just above the harder layer.

Also important to note is that most failures occurred in the storm snow, rather than at the storm snow/old snow interface. For instance, 65% (13/20) of the crown profiles failed in storm snow. Similarly,

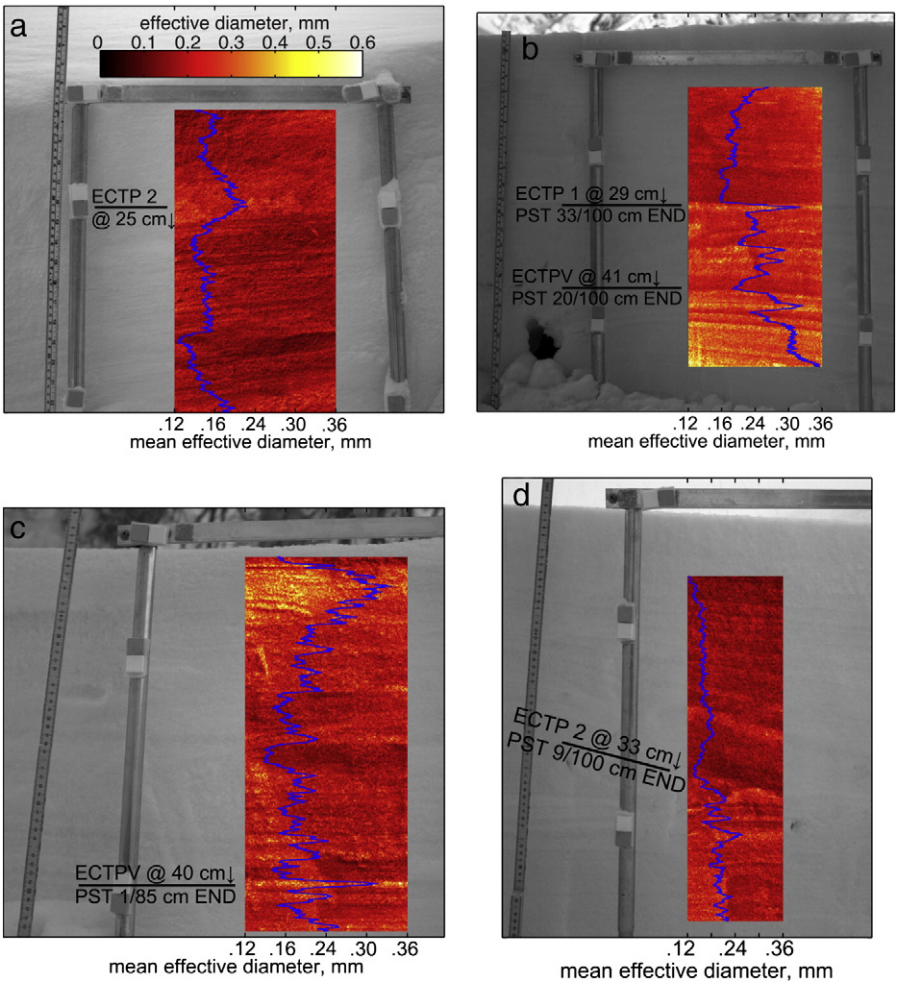

Fig. 9. NIR images of PSTs with failure layers containing nonpersistent crystals. Overlaid on the false-color portion of each image is a graph of the mean effective diameter. The color bar corresponds to the false-color region, which shows effective diameter of individual pixels. Stability test results and fracture planes indicated with black lines. Image dates are: (a) 21 Nov 2010, (b) 6 Dec 2010, (c) 20 Dec 2010, (d) 20 Mar 2011.

avalanche control records from Mammoth show 68% of avalanches failed in storm snow. Storm snow may initially bond well to old snow because most Sierra storms begin with low precipitation rates that gradually increase. Low precipitation rates at the start of a storm allow initial storm layers to strengthen via compaction. Conversely, high precipitation rates overwhelm strengthening from compaction by rapidly increasing stress. The result is stronger snow from the beginning of the storm, when precipitation rates are low, than snow that is deposited later in the storm, during high precipitation rates. Changes such as decreasing temperature may also cause weaker crystals to be deposited in the middle of the storm, rather than at the beginning. A preponderance of failures within the storm snow is contrary to the assumption in Conway and Wilbour (1999) that failures occur at the storm/old snow interface.

6.4. Nonpersistent crystals at failures

The most common nonpersistent crystals found in failure layers in the crown profiles were plates (⊙). The most common nonpersistent crystals found in failure layers in the stability tests were stellars (*). Careful examination of the crown profiles shows that many of the failure crystals were actually sectored plates, rather than simple hexagonal plates. Sectored plates can look very similar to stellars, and both are dominated by plane (i.e. *a*-axis) growth (Magono and Lee, 1966). It is possible that some plates were misclassified in the field as stellars and vice-versa. Either way, plane growth, rather than columnar (*c*-axis) or mixed-axis growth is probably an important characteristic of weak nonpersistent crystals. Plane growth crystals may be especially prone to volumetric collapse since they can be stacked in unstable configurations (Fig. 10), while columnar and mixed-axis crystals pack more tightly.

6.5. Near-infrared images

From the nIR images (Fig. 9), we found thin weak layers, composed of much larger crystals than adjacent layers, in two of the images (b and c). Yet, in the other two images (a and d), the failure layer was indistinguishable from the layer above, but distinguishable from the layer below. In these cases, failure occurs at the interface. This supports evidence from Section 5.4 that shows most crown profiles examined were interface failures. Interface failures are common. For instance, Schweizer and Jamieson (2001) report that 82 of 186 (44%) skier-triggered avalanches in Switzerland and Canada were interface failures.

7. Conclusion

Our results are consistent with predictions of the anticrack model and not consistent with predictions of the simple shear model. Using Propagation Saw Tests and Extended Column Tests, we show that triggering fracture in layers with nonpersistent crystals did not depend on slope angle. This result matches tests on persistent crystals

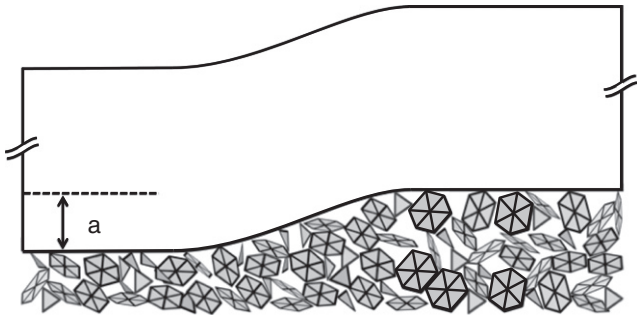

Fig. 10. Collapse wave of amplitude *a* traveling left to right through a layer of sectored plates.

from other studies, suggesting that collapse provides fracture energy in failure layers composed of persistent and nonpersistent crystals. One practical implication of this finding is that stability tests can be conducted in gentler and safer terrain, rather than on steep and potentially dangerous slopes.

Although more measurements are needed, we also report the first collapse amplitude for a failure on nonpersistent crystals, about 1 mm. This collapse amplitude quantitatively shows that nonpersistent crystals collapsed during fracture, just like persistent crystals. *A*-axis crystals were the most common crystals found in failure layers, suggesting they are especially prone to collapse. This result suggests that it is possible to identify potential failure crystals by monitoring hydrometeors throughout a storm.

Evidence from crown profiles and nIR images shows that failures often occurred at interfaces, without weak layers. These interfaces were usually within the storm snow and were marked by a softer layer above and a harder layer below, suggesting that collapse occurred in crystals at the bottom of the slab.

Acknowledgments

The work was supported by the Oak Ridge Institute for Scientific Education and NSF Grants EAR-0537327/EAR-1015057. We thank Joachim Heierli for his assistance in applying the anticrack model and an anonymous reviewer for his or her contribution to our displacement error analysis.

References

American Avalanche Association, 2011. Avalanche Accidents Database.
Bažant, Z.P., Zi, G., McClung, D., 2003. Size effect law and fracture mechanics of the triggering of dry snow slab avalanches. Journal of Geophysical Research 108 (B2), 2119. doi:10.1029/2002JB001884.
Chiaia, B.M., Cornetti, P., Frigo, B., 2008. Triggering of dry snow slab avalanches: stress versus fracture mechanical approach. Cold Regions Science and Technology 53 (2), 170–178. doi:10.1016/j.coldregions.2007.08.003.
Conway, H., Wilbour, C., 1999. Evolution of slope stability during storms. Cold Regions Science and Technology 30 (1–3), 67–77. doi:10.1016/S0165-232X(99)00009-9.
Crocker, J.C., Grier, D.G., 1996. Methods of digital video microscopy for colloidal studies. Journal of Colloid and Interface Science 179 (1), 298–310. doi:10.1006/jcis.1996.0217.
Fierz, C., Armstrong, R.L., Durand, Y., Etchevers, P., Greene, E., McClung, D.M., Nishimura, K., Satyawali, P.K., Sokratov, S., 2009. The International Classification for Seasonal Snow on the Ground, IHP-VII Technical Documents in Hydrology No. 83. UNESCO-IHP, Paris. 90 pp.
Gauthier, D., Jamieson, B., 2008. Evaluation of a prototype field test for fracture and failure propagation propensity in weak snowpack layers. Cold Regions Science and Technology 51 (2–3), 87–97. doi:10.1016/j.coldregions.2007.04.005.
Heierli, J., 2008. Anticrack model for slab avalanche release. Ph.D. Thesis, Universität Karlsruhe, Germany, 113 pp.
Heierli, J., Birkeland, K.W., Simenhois, R., Gumbsch, P., 2011. Anticrack model for skier triggering of slab avalanches. Cold Regions Science and Technology 65 (3), 372–381. doi:10.1016/j.coldregions.2010.10.008.
Heierli, J., Gumbsch, P., Zaiser, M., 2008. Anticrack nucleation as triggering mechanism for snow slab avalanches. Science 321 (5886), 240–243. doi:10.1126/science.1153948.
Hutchinson, J.W., Suo, Z., 1991. Mixed mode cracking in layered materials. Advances in Applied Mechanics 29, 63–191. doi:10.1016/s0065-2156(08)70164-9.
Jamieson, J.B., Johnston, C.D., 1992. Snowpack characteristics associated with avalanche accidents. Canadian Geotechnical Journal 29 (5), 862–866. doi:10.1139/t92-093.
Johnson, B.C., 2001. Remotely triggered slab avalanches. M.Sc. Thesis, University of Calgary, Calgary, AB, Canada, 109 pp.
Johnson, B.C., Jamieson, J.B., Stewart, R.R., 2004. Seismic measurement of fracture speed in a weak snowpack layer. Cold Regions Science and Technology 40 (1–2), 41–45. doi:10.1016/j.coldregions.2004.05.003.
Kruskal, W.H., Wallis, W.A., 1952. Use of ranks in one-criterion variance analysis. Journal of the American Statistical Association 47 (260), 583–621.
Louchet, F., Faillettaz, J., Daudon, D., Bédouin, N., Collet, E., Lhuissier, J., Portal, A.-M., 2002. Possible deviations from Griffith's criterion in shallow slabs, and consequences on slab avalanche release. Natural Hazards and Earth System Sciences 2 (3/4), 157–161. doi:10.5194/nhess-2-157-2002.
Magono, C., Lee, C.W., 1966. Meteorological classification of natural snow crystals. Journal of the Faculty of Science, Geophysics 2 (4), 321–335.
Matzl, M., 2006. Quantifying the stratigraphy of snow profiles. Ph.D. Thesis, Eidgenössische Technische Hochschule, Zürich, Switzerland, 88 pp.
Matzl, M., Schneebeli, M., 2006. Measuring specific surface area of snow by near-infrared photography. Journal of Glaciology 52 (179), 558–564. doi:10.3189/172756506781828412.
McClung, D.M., 1979. Shear fracture precipitated by strain softening as a mechanism of dry slab avalanche release. Journal of Geophysical Research 84 (B7), 3519–3526. doi:10.1029/JB084iB07p03519.
McClung, D.M., 1981. Fracture mechanical models of dry slab avalanche release. Journal of Geophysical Research 86 (B11), 10783–10790. doi:10.1029/JB086iB11p10783.
McClung, D.M., 2005. Dry slab avalanche shear fracture properties from field measurements. Journal of Geophysical Research 110, F04005. doi:10.1029/2005JF000291.
McClung, D.M., 2009. Dry snow slab quasi-brittle fracture initiation and verification from field tests. Journal of Geophysical Research 114, F01022. doi:10.1029/2007JF000913.
McClung, D.M., 2011. The critical size of macroscopic imperfections in dry snow slab avalanche initiation. Journal of Geophysical Research 116, F03003. doi:10.1029/2010jf001866.
McClung, D.M., Schweizer, J., 2006. Fracture toughness of dry snow slab avalanches from field measurements. Journal of Geophysical Research 111, F04008. doi:10.1029/2005JF000403.
Palmer, A.C., Rice, J.R., 1973. The growth of slip surfaces in the progressive failure of over-consolidated clay. Proceedings of the Royal Society of London A 332, 527–548. doi:10.1098/rspa.1973.0040.
Penniman, D., 1986. The Alpine Meadows avalanche trial: conflicting viewpoints of the expert witnesses. 1986 International Snow Science Workshop, pp. 189–194.
Perla, R., 1977. Slab avalanche measurements. Canadian Geotechnical Journal 14 (2), 206–213. doi:10.1139/t77-021.
Reiweger, I., Schweizer, J., 2010. Failure of a layer of buried surface hoar. Geophysical Research Letters 37 (24), L24501. doi:10.1029/2010gl045433.
Roch, A., 1966. Les variations de la resistance de la neige. Scientific Aspects of Snow and Ice Avalanches, pp. 182–195.
Rousselout, M., Durand, Y., Giraud, G., Merindol, L., Daniel, L., 2010. Analysis and forecast of extreme new-snow avalanches: a numerical study of the avalanche cycles of February 1999 in France. Journal of Glaciology 56 (199), 758–770. doi:10.3189/002214310794457308.
Schneebeli, M., 2008. Practice of near-infrared photography of snowpits. Eos, Transactions of the American Geophysical Union 89 (53) Fall Meeting Supplement, Abstract C34A-06..
Schweizer, J., Jamieson, B., 2001. Snow cover properties for skier triggering of avalanches. Cold Regions Science and Technology 33 (2–3), 207–221. doi:10.1016/s0165-232x(01)00039-8.
Schweizer, J., Jamieson, B., 2003. Snowpack properties for snow profile analysis. Cold Regions Science and Technology 37 (3), 233–241. doi:10.1016/S0165-232X(03)00067-3.
Schweizer, J., Jamieson, B., 2010. Snowpack tests for assessing snow-slope instability. Annals of Glaciology 51 (54), 187–194.
Simenhois, R., Birkeland, K., 2009. The extended column test: test effectiveness, spatial variability, and comparison with the propagation saw test. Cold Regions Science and Technology 59 (2–3), 210–216. doi:10.1016/j.coldregions.2009.04.001.
Stethem, C., Perla, R., 1980. Snow-slab studies at Whistler Mountain, British Columbia, Canada. Journal of Glaciology 26 (94), 85–91.
Tape, K., Rutter, N., Marshall, H.P., Essery, R., Sturm, M., 2010. Recording microscale variations in snowpack layering using near-infrared photography. Journal of Glaciology 56 (195), 75–80. doi:10.3189/002214310791190938.
van Herwijnen, A., Heierli, J., 2010. A field method for measuring slab stiffness and weak layer fracture energy. 2010 International Snow Science Workshop. 232-237.
van Herwijnen, A., Jamieson, B., 2005. High-speed photography of fractures in weak snowpack layers. Cold Regions Science and Technology 43 (1–2), 71–82. doi:10.1016/j.coldregions.2005.05.005.
van Herwijnen, A., Jamieson, B., 2007. Fracture character in compression tests. Cold Regions Science and Technology 47 (1–2), 60–68. doi:10.1016/j.coldregions.2006.08.016.
van Herwijnen, A., Schweizer, J., Heierli, J., 2010. Measurement of the deformation field associated with fracture propagation in weak snowpack layers. Journal of Geophysical Research 115, F03042. doi:10.1029/2009jf001515.
Villecrose, J., 2001. Les avalanches de janvier et février 1999 dans les Alpes Du Nord françaises — Contexte nivo-météorologique et comparaison avec les épisodes passés. La Météorologie 32, 11–22.